Model-Based Least Squares Reconstruction of Coded Source Neutron Radiographs: Integrating the ORNL HFIR CG1D Source Model

Hector J. Santos-Villalobos, Jens Gregor, and Philip R. Bingham

***Abstract*—At the present, neutron sources cannot be fabricated small and powerful enough in order to achieve high resolution radiography while maintaining an adequate flux. One solution is to employ computational imaging techniques such as a Magnified Coded Source Imaging (CSI) system. A coded-mask is placed between the neutron source and the object. The system resolution is increased by reducing the size of the mask holes and the flux is increased by increasing the size of the coded-mask and/or the number of holes. One limitation of such system is that the resolution of current state-of-the-art scintillator-based detectors caps around $50\mu m$. To overcome this challenge, the coded-mask and object are magnified by making the distance from the coded-mask to the object much smaller than the distance from object to detector. In previous work, we have shown via synthetic experiments that our least squares method outperforms other methods in image quality and reconstruction precision because of the modeling of the CSI system components. However, the validation experiments were limited to simplistic neutron sources. In this work, we aim to model the flux distribution of a real neutron source and incorporate such a model in our least squares computational system. We provide a full description of the methodology used to characterize the neutron source and validate the method with synthetic experiments.**

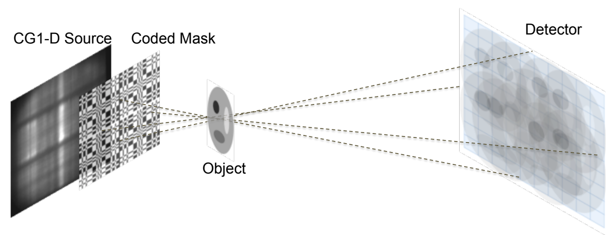

Fig. 1. Coded source imaging system components and geometry. Observe that the holes in the mask generate off-set projections of the object at the detector.

I. Introduction

X-ray and neutron optics both lack ray focusing capabilities. However, an X-ray source can be made small and powerful enough to facilitate high-resolution imaging while providing adequate flux. This is not yet possible for neutrons. One remedy is to employ a computational imaging technique such as coded source imaging (CSI) [1, 2, 3]. Evolved from coded aperture imaging (CAI), where a coded-mask is placed in front of the detector [4], for CSI the coded-mask is placed between the neutron source and the object. As illustrated in Fig. 1, a CSI system is at least composed of (from left to right) a neutron source, the coded aperture mask, the object and corresponding field-of-view aperture, and finally, the detector. Similarly to the classical single pinhole imaging, CSI image resolution is proportional to the size of the apertures of the coded-mask (i.e., the smaller the apertures, the smaller the features the system can resolve). However, in contrast with the classical single pinhole approach, where neutron flux is inversely proportional to the size of the pinhole, for CSI, flux is proportional to the size of the mask. Therefore, neutron flux is kept constant for different aperture sizes in a CSI system. On the other hand, the resolution of the CSI system is still limited by the resolution of the detector. As an example, if the distances from mask to object and object to detector are equal (i.e., 1:1 magnification) and the coded-mask apertures are perfectly registered with the detector pixels, the smallest allowable size for the mask apertures is equal to the size of the detector pixels. In general, it is not practical to achieve perfect alignment between the coded-mask and detector, therefore, more detector pixels are needed per mask holes to comply with Nyquist sampling, which limits even further the size of the mask apertures to at least twice the size of the detector pixels. State-of-the-art scintillator-based detectors currently have a resolution limit of about 50μ, therefore, in order to reach resolutions of 10μ or greater, Bingham et al. proposed a coded source system with magnifications above 10:1 [2].

In previous work, we have documented the advantages of a model-based least squares algorithm over direct convolution as well as blind deconvolution wrapped in a maximum-likelihood framework for the reconstruction of coded source radiographs [3]. We used simulated data experiments to show that the least squares method outperformed the other methods with respect to image quality and reconstruction precision because of the modeling of the system components, such as the neutron source, the distribution of flux through the detector pixels, the system field-of-view, imperfections of the coded-mask, etc. [3] However, in these experiments, the source modeling was limited to uniform and Gaussian neutron sources which, as shown in Fig. 2, do not represent real life neutron sources. We argue that the greatest challenge associated with successful reconstruction of real data from a complex source such as the HFIR CG-1D is to precisely model the neutron rays flux

Manuscript received November 30th, 2012. Research supported by the United States Department of Energy, Early Career Award Program.

P. R. Bingham is with the Oak Ridge National Laboratory, Oak Ridge, TN 37931 USA (phone: 865-574-5680, e-mail: binghampr@ornl.gov).

H. J. Santos-Villalobos is with the Oak Ridge National Laboratory, Oak Ridge, TN 37931 USA (phone: 865-574-0215, e-mail: hsantos@ornl.gov).

J. Gregor is with the University of Tennessee, Knoxville, TN 37996 USA (phone: 865-974-4399, e-mail: jgregor@eecs.utk.edu).

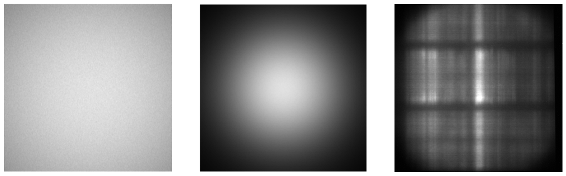

(a) (b) (c)

Fig. 2. Illustration of neutron Sources: synthetic (a) uniform and (b) Gaussian sources, and (c) actual HFIR CG1-D source imaged with a 2mm pinhole.

distribution at each coded-mask hole.

II. Image Reconstruction

A. Deconvolution approach

CAI techniques apply to CSI, consequently, coded aperture patterns such as Modified Uniformly Redundant Array (MURA) and deconvolution reconstruction approaches [5] can be seamlessly employed in CSI. Each MURA mask hole generates an offset projection of the object at the detector. If the projections do not overlap, the object radiograph is reconstructed with the sum of all registered projections. In general, CSI systems produce overlapping projections, which require deconvolution for image reconstruction. This model can be expressed as

$$P = O * A + \eta, \tag{1}$$

where P is the measured encoded radiograph, O is the object to reconstruct, A is the MURA aperture mask, and η is uncorrelated noise. Image reconstruction is then reduced to an inverse problem, where we need to find O given P, A, and *a priori* η. The typical reconstruction approach is direct deconvolution by kernel G. That is,

$$\hat{O} = P * G = (O * A + \eta) * G = O + \eta * G. \tag{2}$$

Note that this approach adds a noise component to the reconstructed signals. The noise can be suppressed by exposing the object for a second time using a complementary aperture mask A_c, which satisfies $A_c = \neg A$ and $A * G = A_c * (-G) = \delta$; with the exception that for both A_c and A the central aperture remains closed or zero [6]. This method is known as the mask-antimask approach. Then, the reconstructed object is approximated by

$$\begin{aligned} \hat{O} &= \frac{1}{2}(P_A - P_{A_c}) * G \\ &= \frac{1}{2}(O * A + \eta - (O * A_c + \eta)) * G \\ &= \frac{1}{2}(O * (A * G) + O * (A_c * -G)) \\ &= O. \end{aligned} \tag{3}$$

This model holds if and only if the neutron illumination source uniformly emits rays parallel to the imaging axis, A and A_c are perfectly aligned, and the coded aperture masks are free of manufacturing imperfections, and that the system point spread function $A * G = \delta$ [3]. Observe that these requirements are not fulfilled in a magnification modality, where near-field imaging and divergent rays are needed. In addition, the flux distribution in actual neutron sources is far from ideal. As we will describe shortly, a model-based iterative reconstruction algorithm is better suited to address these challenges.

B. Model-based iterative reconstruction

SIRT is a well-known iterative algorithm for reconstruction of tomographic images from projections. Although our problem is not tomographic, it is mathematically of a similar nature. We use a modified version of SIRT called PSIRT for which near-optimal relaxation can be achieved [7]. The reconstruction is subjected to minimum norm based Tikhonov regulatization [8].

Let $\boldsymbol{A}$ denote the system matrix which models the beamline including the source flux variations, and let $\boldsymbol{x}$ and $\boldsymbol{y}$ denote the vectors representing the unknown image and the acquired coded source projection data, respectively. Reconstruction can then be described as a matter of solving the least squares problem

$$\boldsymbol{x}^* = \arg\min_{\boldsymbol{x}} \|\boldsymbol{A}\boldsymbol{x} - \boldsymbol{y}\|^2_{\boldsymbol{R}} + \beta \|\boldsymbol{x}\|^2_2 \tag{4}$$

where $\boldsymbol{R}$ is a diagonal matrix of inverse row sums of $\boldsymbol{A}$. Hyperparameter β establishes the trade-off between the data term (left norm) and the model term (right norm).

The regularized PSIRT algorithm solves (4) by means of the iterative scheme

$$\boldsymbol{x}^{(k+1)} = (1 - \alpha\beta\mathrm{p})\boldsymbol{x}^{(k)} + \alpha\mathrm{p}\ \boldsymbol{A}'\boldsymbol{R}(\boldsymbol{y} - \boldsymbol{A}\boldsymbol{x}^{(k)}) \tag{5}$$

where $\mathrm{p} = 1/\|\boldsymbol{A}\|_1$, i.e., p represents the inverse of the largest column sum of $\boldsymbol{A}$, and $0 < \alpha < 2$ is a user-defined relaxation parameter. It can be shown that $\alpha = 2/(1 + 2\beta\mathrm{p})$ is near-optimal in that when $\beta\mathrm{p}$ is small, it leads to two times speed-up in terms of needing about half as many iterations to achieve the same minimization of (4) as required without use of relaxation.

Moving toward the reconstruction of real coded neutron radiographs, we have integrated a more complex mask model to our least squares algorithm. This is required in order to model the neutron source as viewed through the coded-mask holes. The HFIR CG-1D imaging beamline has the neutron particles travel through a system of guides where each mask hole has a different view of the guide mirrors and a unique non-uniform flux distribution. Therefore, a cell element a_{ij} of $\boldsymbol{A}$ is given by

$$a_{ij} = \sum_{n=1}^{N} A_n c_{n,i,j} \phi_{n,i,j},\ i \in [1, M],\ j \in [1, Q]$$

where M and Q are the number of detector and object pixels, respectively, A_n is an element of the coded aperture (i.e., 1 if the mask is open and 0 otherwise), $c_{n,i,j}$ denotes an interpolation coefficient to adjust the contribution of neighboring pixels in a discrete space, and $\phi_{n,i,j}$ is the neutron flux or the probability of a neutron particle passing through mask hole A_n, detector pixel i and object pixel j. Note that for a uniform neutron source the flux term is constant $\phi_{n,i,j} = \phi$. For non-uniform sources where all coded aperture mask holes have an equivalent flux angular distribution (e.g., Gaussian source), the flux term is redefined as $\phi_{n,i,j} = \phi_{i,j}$, where the tuple i, j index the angular flux variation.

Note that it is impractical to empirically measure the flux distribution for all the holes in a MURA mask–most coded-masks contain hundreds and even thousands of holes. Therefore, as we will explain shortly, our strategy is to estimate the mask holes flux distribution from a limited set of empirical measurements.

C. Multi-source modeling

In order to capture the flux variations of the HFIR source, we sample it using a small diameter aperture from $500\mu m$ to $2mm$. We call this aperture the characterization aperture. Since the view of the source depends on the placement of this aperture, we compare three different configurations. The simplest configuration consists of sampling just the central view, which assumes $\phi_{n,i,j} = \phi_{i,j}$. The other two configurations are based on bilinear interpolation of the four nearest views from 3×3 and 5×5 regular view grids, respectively.

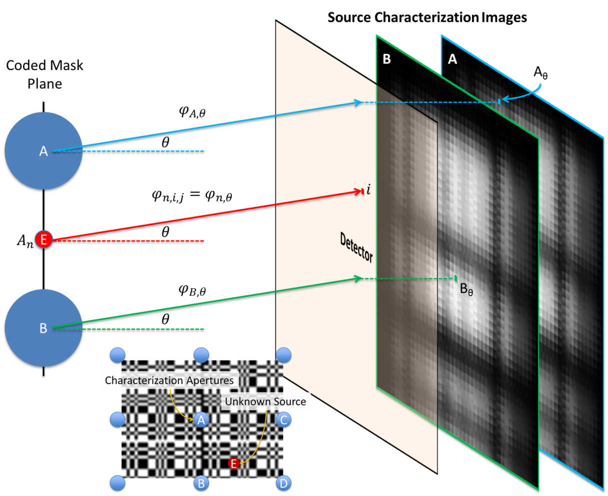

Fig. 3. Side view illustration of source flux estimation from empirical samples. The open beam radiographs for characterization apertures A and B are at the same detector plane, they are shown at different depths for illustration purposes. The bottom left figure illustrates a 3×3 characterization configuration. Note that the outer characterization apertures are placed to guarantee full enclosure of the source.

Fig. 3 illustrates the new flux model for a 3×3 configuration as shown at the bottom left of the figure. The mask aperture E is estimated from the characterization apertures at A, B, C, and D (in the side view A and B are only shown). The flux distribution is given by

$$\phi_{n,i,j} = \phi_{n,\theta} = \sum_{k \in \{A,B,C,D\}} w_{n,k} \times p_{k,\theta},$$

where θ is the direction between detector and object pixels i and j, respectively, weights w_k sum to 1, w_k is inversely proportional to the distance between the mask aperture A_n (e.g., E) and characterization aperture k (e.g., A, B, C, or D), and $p_{k,\theta}$ is the source normalized empirical flux with direction θ as estimated with characterization aperture k. As shown in Fig. 3, the rays traced for the characterization apertures have the same direction θ as the ray for which we want to estimate flux. Note that the same source characterization images can be used for different mask and objects as long as the mask position remains unchanged and the mask size fit inside the outer characterization apertures.

III. Simulations and Results

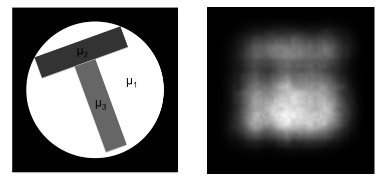

(a) (b)

Fig. 4. (a) **T** object used in Monte Carlo simulations. The open region has an expected attenuation coefficient of $\mu_1 = 1.0$. The **T**'s top and bottom components have attenuation coefficients $\mu_2 = 0.2$ and $\mu_3 = 0.4$, respectively. (b) Coded source projection of **T** object.

The new model was tested with Monte Carlo simulations with the neutron ray tracing software McStas [9]. The HFIR CG1-D beamline was modeled in McStas in order to obtain a highly textured illumination pattern. The source characterization configurations were all centered at the beam axis (i.e., z-axis) and the selected aperture sizes were $500\mu m$, $1mm$, and $2mm$. For the results below, we imaged the **T** object shown in Fig. 4(a). The object was placed $1m$ from the mask and $4m$ from the detector for an effective 5:1 object magnification. The imaging was performed with a 61×61 MURA coded aperture with $100\mu mm$ holes, a $2.0mm$ field-of-view aperture, and a 361×361 detector with $100\mu m$. The coded source in Fig. 4(b) was reconstructed with direct convolution and the improved model-based iterative reconstruction algorithm.

As shown in Fig. 5(a), direct deconvolution reconstruction with a single mask is negatively impacted by the nonuniform illumination of the CG1-D source. The reconstructed image suffer from illumination fluctuations and low contrast. On the other hand, although the mask-antimask approach is not artifact free, Fig. 5(b) shows that it suppresses most of the near-field imaging issues of the single mask approach. However, recall that the mask-antimask approach requires a second exposure with an accurately registered complementary mask. Also, as we will show shortly, the mask-antimask approach offers low separation between the reconstructed attenuation values.

A. Results

We aim to produce image quality reconstructions comparable to or better than that of the two-exposure mask-antimask convolution-based approach (See Fig. 5(b)). After a qualitative assessment of the results in Fig. 5, it is evident that PSIRT outperform the single-mask convolution approach. However, it is also clear that the contrast of PSIRT reconstructions is lower than that of the two-exposure mask-antimask approach. This was quantitatively confirmed with the attenuation distribution (i.e., image pixel intensity histogram) of the reconstructed object as shown in Fig. 5(c) and 5(l). The object's expected attenuation values μ_1 (blue dot), μ_2 (red dot), and μ_3 (green

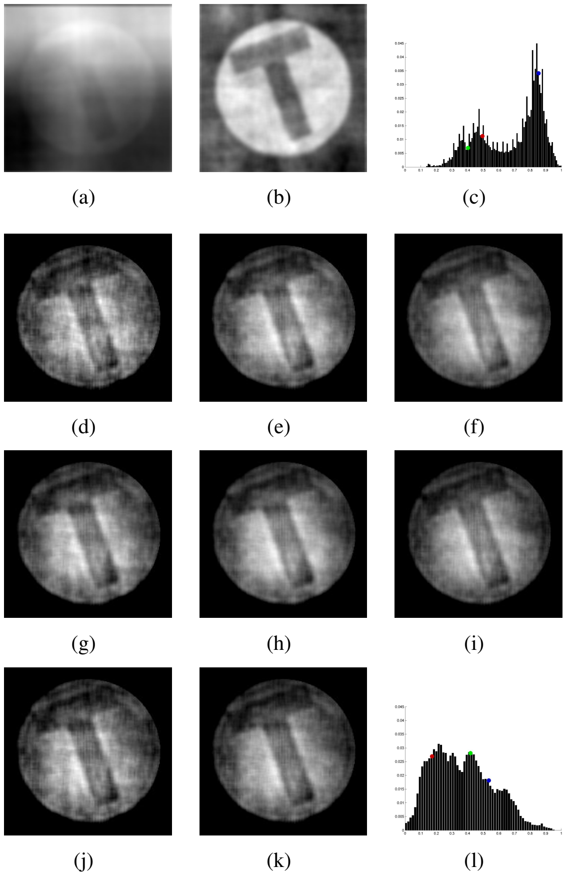

Fig. 5. Direct deconvolution reconstruction with: (a) single mask and (b) mask-antimask approaches. (PSIRT reconstruction for the following configurations: (d) $1 \times 1\ 0.5mm$, (e) $1 \times 1\ 1mm$, (f) $1 \times 1\ 2mm$, (g) $3 \times 3\ 0.5mm$, (h) $3 \times 3\ 1mm$, (i) $3 \times 3\ 2mm$, (j) $5 \times 5\ 0.5mm$, and (k) $5 \times 5\ 1mm$. (l) Pixel intensity histogram of (k).

dot) are 1.0, 0.2, and 0.4, respectively. Note that the convolution approach better reconstruct the open area (i.e., μ_1) allowing better contrast between the open area and the **T** object. Although PSIRT did not generate reconstructions with better contrast for the **T** object, in general, there was a more accurate reconstruction of the **T** object attenuation values μ_1 and μ_2.

Beside comparing PSIRT to the traditional approach, we also want to select the best characterization aperture configuration. For this, we employed the Contrast Discrimination Function (CDF) as a measurement of image quality. Fig. 6 shows

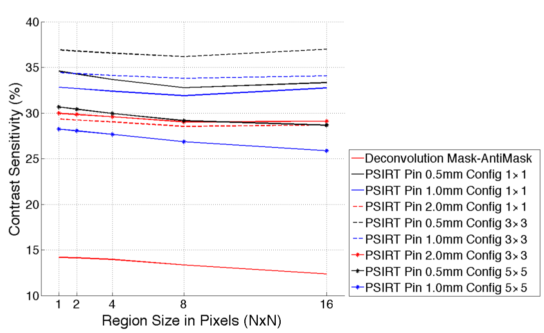

Fig. 6. CDF curves for reconstructed images.

the CDF curves for several multi-source PSIRT model configurations and for the mask-antimask convolution approach (i.e., smaller contrast sensitivity percentage is better). The results show that there is a trade-off between characterization aperture size and source sampling and image quality. Smaller characterization apertures image the source better, but also increases the complexity of the reconstruction given that the optimization needs to solve for higher frequency features. On the other hand, for large apertures important source flux features are lost and consequently limiting the validity of the PSIRT model. For the tested CSI setup, the best performance was obtained from the $5 \times 5\ 1mm$ characterization aperture configuration.

IV. Conclusion

In order to perform magnified CSI on real sources, we have incorporated a multi-source flux characterization feature to our PSIRT least squares model. Our synthetic experiments show that the new PSIRT model outperforms the single mask convolution approach, but it is outperformed contrast-wise by the mask-antimask convolution approach. Nevertheless, the least squares approach produced the most accurate attenuation value reconstructions for the object of interest. We are currently working on improving the contrast of the PSIRT reconstruction by improving the least squares model. We have shown that there is a trade-off between the number of characterization sources, aperture size, and image quality. We need to further study these trade-offs in search for a generalized CSI design method.

Acknowledgment

Funding for this effort came from the U.S. Department of Energy through an early career award out of the Office of Basic Energy Sciences, which also sponsors both the High Flux Isotope Reactor and the Center for Nanophase Materials Sciences at Oak Ridge National Laboratory where portions of this research were performed.

References

[1] A. L. Damato, B. K. P. Horn, and R. C. Lanza, *Coded source imaging for neutrons and x-rays*, IEEE Nuclear Science Symposium Conference, pp. 199–203, October 2006

[2] P. Bingham, H. Santos-Villalobos, and K. Tobin, *Coded source neutron imaging*, SPIE Machine Vision Applications IV, vol. 7877, San Francisco, CA, USA February 2011.

[3] H. Santos-Villalobos, P. Bingham, and J. Gregor, *Iterative reconstruction of coded source neutron radiographs*, IEEE Transactions on Nuclear Science, vol. 60, no. 3, pp. 1624–1631, 2013.

[4] E. Fenimore and T. M. Cannon, *Coded aperture imaging with uniformly redundant arrays*, Applied Optics, vol. 17, pp. 337–34, 1978.

[5] S. R. Gottesman and E. E. Fenimore, *New family of binary arrays for coded aperture imaging*, Appl. Opt., vol. 28, no. 20, pp. 4344–4352, Oct 1989.

[6] R. Accorsi and R. C. Lanza, *Near-field artifact reduction in planar coded aperture imaging*, Applied Optics, vol. 40 no. 26, pp. 4697–4705, 2001

[7] J. Gregor and T. Benson, *Computational analysis and improvement of SIRT*, IEEE Trans. Medical Imaging, vol. 27, pp. 918–924, 2008.

[8] J. Gregor, "Algorithmic improvements to SIRT with application to X-ray CT of luggage," *Third Intl. Conf. Image Formation in X-ray Computed Tomography* (Salt Lake City, Utah), 2014.

[9] K. Lefmann and K. Nielsen, *McStas, a General Software Package for Neutron Ray-tracing Simulations*, Neutron News, 10(20), pp. 20–23, 1999.